Journal of Colloid and Interface Science 607 (2022) 1661–1670

Contents lists available at ScienceDirect

Journal of Colloid and Interface Science

journal homepage: www.elsevier.com/locate/jcis

Controlling supraparticle shape and structure by tuning colloidal interactions

Wendong Liu [a,b], Michael Kappl [b,*], Werner Steffen [b], Hans-Jürgen Butt [b]

[a] School of Chemical Engineering, Dalian University of Technology, Linggong Road 2, Dalian 116024, PR China
[b] Department of Physics at Interfaces, Max Planck Institute for Polymer Research, Ackermannweg 10, D-55128 Mainz, Germany

GRAPHICAL ABSTRACT

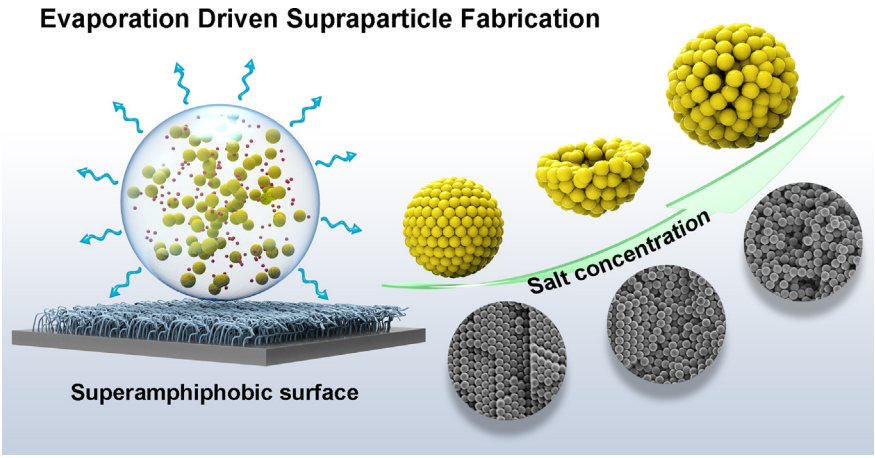

ARTICLE INFO

Article history:
Received 15 July 2021
Revised 3 September 2021
Accepted 6 September 2021
Available online 8 September 2021

Keywords:
Supraparticle
Evaporation
Crystallization
Forces
Superamphiphobic surface
Colloid
Assembly

ABSTRACT

Hypothesis: Assembly of colloids in drying colloidal suspensions on superhydrophobic surface is influenced by the colloidal interactions, which determine the shape and interior structure of the assembled supraparticle. The introduction of salt (electrolyte) into the assembly system is expected to influence the colloid interactions and packing during the evaporation process. Hence, both the outer shape and internal structure of supraparticles should be controlled by varying salt concentrations.
Experiments: Suspensions of electrostatically stabilized polystyrene particles with specified salt concentrations were chosen as model systems to conduct the evaporation on a superhydrophobic surface. A systematic study was performed by regulating the concentration and valency of salt. The morphology and interior of supraparticles were carefully characterized with electron scanning microscopy, while the colloidal interaction was established using colloidal probe atomic force microscopy.
Findings: Supraparticles displayed a spherical-to-nonspherical shape change due to the addition of salts. The extent of crystallization depended on salt concentration. These changes in shape and structure were correlated with salt-dependent single colloid interaction forces, which were not previously investigated in detail in radially symmetric evaporation geometry. Our findings are crucial for understanding assembly behavior during the drying process and offer guidance for preparing complex supraparticles to meet specific applications requirement.

* Corresponding author.
E-mail address: kappl@mpip-mainz.mpg.de (M. Kappl).

https://doi.org/10.1016/j.jcis.2021.09.035
0021-9797/

1. Introduction

Supraparticles are assemblies of primary nano- or microscale colloids with a typical size from several tens of microns to several hundreds of microns [1,2]. Colloids agglomerate into larger supraparticles, which are easier to handle and recover and have combined functionalities of nano- and/or microscale colloids, *e.g.,* high specific surface area, intrinsic material properties, catalytic activity, *etc.*[1] Benefiting from the synergism, coupling, and colocalization of colloids, supraparticles may perform improved functions while reducing the hazards caused by the high mobility of nanoscale colloids [1,3–5]. Therefore, supraparticles have attracted considerable attention and shown specific structure and applications [6,7], *e.g.,* heterogeneous catalysis [8,9], photonic materials [10–12], drug delivery [13–15], or energy production-related materials [16–19].

Most supraparticles are fabricated in solution, either by kinetics or thermodynamics-controlled growth or by template-based synthesis [1,20–28]. These approaches have the advantage of large-scale production. Nevertheless, they depend on additional chemicals, especially for structural engineering. The chemicals need to be removed from the assemblies for disposal, which may harm the environment and consume additional resources. With the aim of reducing or completely avoiding the use of hazardous solvents, emulsifiers, templates, or any other processing liquid, researchers introduced evaporation-driven self-assembly as a promising method for supraparticle preparation [29,30]. On surfaces, droplets usually assume a shape of spherical cap, except for the case with a contact angle of 90°, which forms a hemisphere. The nonradial symmetric shape undergoes anisotropic evaporation and induces internal colloids to aggregate at the three-phase line to form ring-like or doughnut-like structures (coffee-stain effect) [31,32]. In contrast, on super liquid-repellent surfaces (superhydrophobic, superoleophobic, and superamphiphobic surfaces), suspension droplets have a nearly spherical morphology. This spherical morphology results from the large contact angle (CA > 150°) and small roll-off angle (tilt angle less than 10°) [33–38]. As contact line pinning can be neglected and surface tension forces dominate over the viscous forces, the droplet on super liquid-repellent surfaces shrinks virtually simultaneously in all directions. Even though the evaporation of a droplet on a superhydrophobic surface will not be fully isotropic [31,32], the minimal contact area ($\ll V^{2/3}$, where V is the volume of the drop) between the liquid and solid and the porous structure of the liquid-repellent surface will also allow the evaporation into the highly porous substrate side, resulting in an almost radially symmetric evaporation [2,39,40]. This makes the process like spray drying, but with the advantage that the kinetics can be slowed down and direct observation of the process is straightforward.

Recently, researchers have utilized this evaporation-driven self-assembly approach for the fabrication of supraparticles from monotonic or binary dispersions of nanoscale colloids. They demonstrated the formation of highly porous structures, with broad potential applications of such supraparticles in catalysis [2,40,41].

To date, research on supraparticles has mainly focused on the properties and functions of the obtained supraparticles but not the structure formation process. In our previous work, we have demonstrated that specific drying conditions lead to the segregation of different size particles during the drying of binary colloidal dispersions [39]. In this case, the supraparticles exhibited a core–shell morphology. The outer layer was mainly occupied by small colloids that formed a close-packed crystalline structure. Toward the core, the concentration of large colloids increased, and they packed amorphously. The extent of this stratification decreased when the evaporation rate was reduced [39]. Sperling *et al.* reported the effect of ionic strength on the apparent shape of supraparticles prepared by evaporating a silica suspension droplet on a superhydrophobic surface [42]. By increasing the ionic strength, the supraparticle buckled due to the accumulation of silica nanoparticles at the liquid–air interface. Buckling was stronger with increasing ionic strength. At a high salt concentration (25 mM), highly anisometric (boat-like) supraparticles were obtained. These observations indicate that electrostatic double-layer forces influence structure formation in drying droplets of colloidal suspensions.

Here, we investigate in detail the influence of intercolloid forces on the structure and shape of supraparticles. We experimentally explored the drying process of polystyrene (PS) colloids dispersed in aqueous electrolytes with different salt concentrations. Of particular interest is the crystallization of monodisperse PS colloids within the supraparticle, i.e., whether they form completely crystalline supraparticles or if the degree of crystallization changes with salt concentration. By measuring the interaction between individual colloids with colloidal probe atomic force microscopy (AFM), we can correlate changes in the structure and shape of the supraparticle with the interaction between individual colloids at different salt concentrations. Our results show that the change in the interaction between colloids caused by the screening of electrostatic repulsion by adding salt has a drastic effect on the structure and morphology of the supraparticles. An improved understanding of the assembly process in drying droplets on superamphiphobic surfaces will be beneficial to specific supraparticle fabrication, and extend new research and application areas in colloid and interface science.

2. Materials and methods

2.1. Materials and chemicals

Methyl trichlorosilane (TCMS, 99%) and hexadecane (Reagent Plus, 99%) were purchased from Aldrich. 1*H*,1*H*,2*H*,2*H*-Perfluorodecyltrichlorosilane (PFDTS, 96%) was purchased from Alfa Assar. *N*-Hexane (95%) was purchased from Fisher Chemical. Sodium chloride (NaCl, ≥ 99.5%) and calcium chloride ($CaCl_2$, ≥98%) were provided by Carl Roth GmbH + Co. KG. VWR CHEMICALS provided toluene, acetone, and absolute ethanol. Ultrapure water with a resistivity of 18.2 MΩ·cm was produced using a Sartorius Arium 611 VF water purification system. Glass sides 25 mm × 75 mm in size were provided by Menzel-Gläser, Germany. Polystyrene colloids (negatively charged, ≈ − 48 mV, with –COOH groups on the surface) with a diameter of 440 nm and 4 μm were prepared by the copolymerization of styrene and acrylic acid using surfactant-free emulsion polymerization [43]. The molar ratio of styrene to acrylic acid in both cases was maintained at 60:1 to achieve similar surface chemistry, and the as-prepared colloids were purified by several cycles of centrifugation and redispersion in ultrapure water.

2.2. Preparation of silicone nanofilaments-based superamphiphobic surfaces

The superamphiphobic surfaces were prepared by the grow-from method [2,44,45]. In brief, cleaned glass slides were treated with oxygen plasma (30 W for 2 min). Then activated substrates were immersed in a mixture of TCMS (250 μL) and toluene (360 mL, 166 ppm water) for 12 h to graft silicone nanofilaments. The water concentration in toluene was evaluated using a Karl Fis-

cher coulometer (Mettler Toledo C20 Compact KF coulometer). The silicone nanofilaments-grafted glass slides were again activated with oxygen plasma (120 W for 2 min) and immersed in a mixture of PFDTS (100 μL) and hexane (120 mL) for 30 min to further reduce the surface tension to achieve superamphiphobicity. The obtained silicone nanofilament-grafted glass was homogeneous over a large area (Fig. S1a,b). Water and hexadecane droplets formed spherical shapes. Water droplets possessed a static contact angle over 162° (Fig. S1c) with a roll-off angle of approximately 2°, while hexadecane droplets had a contact angle of approximately 156° (Fig. S1d) with a roll-off angle of approximately 8° at a volume of 5 μL.

2.3. Evaporation of PS suspension droplets on superamphiphobic surfaces

Mixtures of PS colloids with a diameter of d = 440 nm (polydispersity index = 0.088 ± 0.023) and NaCl were prepared. The volume fraction (vol%) of PS colloid in the water was fixed at 8%. The concentration of NaCl in the mixture was 0 μM, 1 μM, 5 μM, 10 μM, 50 μM, 100 μM, 500 μM, 1 mM, 5 mM, 10 mM, 50 mM, and 100 mM. Approximately 2 μL of these suspensions were dropped onto the superamphiphobic surface. Drops were evaporated at 22 °C, either under ambient conditions (relative humidity 32%) or at a relative humidity of 96% (measured with a TFA Digital Thermo-Hygrometer). High humidity was achieved by putting several opened water bottles around the superamphiphobic substrates in a chamber and allowing the system to equilibrate for approximately 0.5 h before placing the drop.

2.4. Measurement of colloidal interaction

The forces between individual PS colloids were measured using colloid probe AFM [46]. As the colloids need to be mounted onto AFM cantilevers under an optical microscope, we used larger PS particles with diameters of 4 μm, which were prepared by using PS particles from the previous synthesis as seeds and repeating the same synthesis procedure for several cycles. The colloids were attached to AFM cantilevers (Bruker NP-O) with a nominal spring constant of 0.12 N/m using a micromanipulator (Narishige MMO, Narishige, Tokyo, Japan) using a two-component epoxy glue (UHU endfest, Henkel, Germany) to form colloidal probes. The spring constant for each probe was measured using the thermal noise method [47] integrated into JPK III Nanowizard AFM software. The probes were mounted to the liquid cell holder of a JPK Nanowizard III AFM (JPK Instruments, Berlin, Germany). A small droplet of PS colloid dispersion was deposited on a glass slide that had been modified with 3-aminopropyltriethoxysilane to render the glass surface positively charged and improve attachment of the PS particles. After drying, the colloid attachment to the glass substrate was strong enough to allow the exchange of electrolyte solution in the liquid cell without washing off the particles. The glass slides were mounted under the AFM on top of an inverted optical microscope to form the bottom of the liquid cell. The colloidal probe was roughly positioned above an area that was covered by a sub-monolayer of PS particles on the glass slide using the micrometer screws of the microscope stage. To locate the exact position of individual PS particles, we used the AFM to record a force map by taking force curves on a $10 \times 10\ \mu m^2$ area with a raster of 32×32 points. Then 25 force curves were recorded on top of individual PS particles. The AFM raw data (vertical deflection signal in volts vs. z piezo position) were converted into force vs. distance curves and averaged using a in-house software. The averaged force-distance curves were then fitted with the DLVO equation for the force between two spheres of radius R:

$$F(D) = \frac{2\pi\varepsilon\varepsilon_0 R\psi^2}{\lambda_D} e^{-\frac{D}{\lambda_D}}\left[1 - e^{-\frac{D}{\lambda_D}}\right] - \frac{A_H R}{12D^2} \quad (1)$$

where ψ is the surface potential, D is the distance between the surfaces of the spheres, λ_D is the Debye length and A_H is the Hamaker constant [48]. The Debye length is given by:

$$\lambda_D = \sqrt{\frac{\varepsilon\varepsilon_0 k_B T}{2 \cdot 10^3 N_A e^2 I}} \quad (2)$$

Here, $k_B$is the Boltzmann constant, T is the temperature, e is the elementary charge, and N_A is the Avogadro number. I is the molar ionic strength of the electrolyte given by:

$$I = \frac{1}{2}\sum_{i=1}^{n} c_i \varkappa_i^2 \quad (3)$$

Where, the prefactor one half accounts for the inclusion of both cations and anions, c_i is the molar concentration of ion i(M, mol/L), $\varkappa_i$ is the charge number of that ion, and the sum is taken over all ions in the solution. For a 1:1 electrolyte such as sodium chloride, where each ion is singly-charged, the ionic strength is equal to the concentration. As a Hamaker constant, we used a fixed value of 10^{-20} J [49]. To account for surface roughness of the PS colloids, we allowed for an additional positive offset of D, which was introduced as additional fit parameter. Without this offset, which resulted in values between 0 nm and 4 nm from the fitting results, it would not have been possible to match the attractive van der Waals part of the force curves in all the fits. Note that the surface potential of the PS colloids in AFM measurements is different from that measured with a Zetasizer for high salt concentration. One reason may be that we have used the constant potential boundary condition for our calculations for direct comparison of the values. When the colloids are brought in close contact at high salt concentration, the interaction may be intermediate between the constant charge and constant potential cases (charge regulation) which can lead to a reduction of the zeta potential [50]. The Debye length and surface potential of the PS colloids were calculated by fitting the experimental results.

2.5. Characterization

The structure of silicone nanofilaments and supraparticles was imaged by scanning electron microscopy (SEM, low voltage LEO 1530 Gemini, Germany). The samples were sputter-coated with a 7 nm layer of Pt using a BalTec MED 020 modular high-vacuum coating system before taking images to avoid charge buildup. Static and roll-off angles of 5 μL water and hexadecane droplets on the nanofilament-based superamphiphobic surfaces were measured with a Dataphysics OCA35 goniometer (Data Physics instruments GmbH, Germany). Optical micrographs were taken by an optical microscope (Carl Zeiss Axiotech Vario 100HD). The polydispersity and zeta-potential of the prepared PS colloids were characterized by dynamic light scattering (Malvern Zetasizer Nano S90) and the M3-PALS technique (Malvern Zetasizer Nano Z), respectively.

Colloidal suspension droplets were evaporated on a nanofilament-based superamphiphobic surface at 22 °C and a relative humidity RH = 32%. As the radius of the droplet ($r \leq 770\ \mu m$) is lower than the capillary constant of $\kappa = 2.7$ mm, the deposited suspension drop has a nearly spherical shape. The volume of spherical droplets, which evaporate by diffusion-limited evaporation, decreases according to $V^{2/3} = \alpha t$, with the evaporation speed α in units of $\mu m^2/s$. The relationship is valid if the matter exchange between the liquid surface and the vapor is diffusive [51]. For the evaporation of a droplet on a superamphiphobic surface, the evaporation speed was calculated by Picknett and Bexon [52]:

$$\alpha_{sessile} = \left(\frac{8\pi}{3}\right)^{2/3} \frac{D_{air} m \Delta P}{\rho k_B T} \frac{f}{\beta^{\frac{1}{3}}} \quad (4)$$

with $\beta = (1 - cos\theta)^2(2 + cos\theta)$ with the contact angle θ, and $f = 0.00008957 + 0.633\theta + 0.116\theta^2 - 0.08878\theta^3 + 0.01033\theta^4$ for θ (rad) above 10°. To obtain evaporation speed values, we tracked the droplet evaporation with a side-view camera (IDS uEye USB camera) and calculated the changes in $V^{2/3}$ with time. Then the evaporation speed was obtained by a linear fitting of the $V^{2/3}$ vs. t plot.

3. Results and discussion

3.1. Structure and morphology of supraparticles as a function of salt concentration

Complete drying of a colloidal suspension drop (≈ 2 μL) took approximately 24 min (Fig. 1a). The changes in the horizontal and vertical diameters during drying are shown in Fig. 2 and S2; the insets represent side view images of the final supraparticles. At the early stage, the droplets are spherical. The vertical diameter is slightly smaller than the horizontal diameter as a result of a small deformation due to gravity and a possible systematic error in accurately measuring the drop height due to its shadow at the lower end. The droplets all evaporate at a similar rate of approximately 800 $\mu m^2/s$ and the evaporation of liquid in all cases is isotropic (the horizontal and vertical diameters decrease at a similar rate). For distilled water and salt concentrations ≤ 10 μM, PS suspension droplets evaporate isotropically until the end, resulting in spherical supraparticles (Fig. 2a,b and S2a-c). The resulting supraparticles have a nearly spherical morphology (Fig. 1c). Since the droplet shrinks virtually simultaneously in all directions with no contact line pining (Fig. 1b), and the highly porous superamphiphobic surfaces will also allow evaporation from the bottom side, we expect only minor liquid flow in the suspension droplet. The surface of the supraparticle consists of large close-packed crystalline areas with some line and dot defects (Scanning electron microscopy (SEM) images in Fig. 1d and 3a2). The crystalline order at the surface correlates with the strong iridescence of the final supraparticle (top view optical images Fig. S3) and iridescence is already visible during the drying process itself, indicating order formation in the early stage of the drying process.

SEM images of cross-sections reveal a core–shell structure (Fig. 1e). The outer shell exhibits highly ordered crystalline structure (Fig. 1f), whereas the core consists of randomly arranged PS colloids (Fig. 1g). The thickness of the outer crystalline layer is approximately 44% of the supraparticle radius, which implies that the crystalline structure occupies approximately 82–85% of the supraparticle volume.

When the NaCl concentration increases, the supraparticles change significantly. The iridescence of the dried supraparticles (Fig. S3) indicates that the formation of crystalline structures starts to diminish for salt concentrations above 1 mM. For 5 mM and 10 mM NaCl, structural colors could still be observed, but the area and intensity of iridescence were much smaller. When further increasing the NaCl concentration to 50 and 100 mM, no iridescent color was found, indicating the loss of crystalline order. The shape of the supraparticle was affected as well. For NaCl concentrations of 50 μM to 10 mM, supraparticles were no longer spherical. We observed flattening or inward buckling at the bottom side that was in contact with the substrate (Fig. 2 and S2e-k). According to the drying curves, toward the end of the drying phase, the vertical diameter shrank more than the horizontal diameter due to flattening or buckling on the lower side. When the salt concentration exceeded 50 μM, the droplet started to deform at the late stage of evaporation. The vertical diameter decreased faster than the horizontal diameter (Fig. S2e-h). This anisotropy became more pronounced as the NaCl concentration reached 1 mM and above (Fig. S2i-k). A typical example is 5 mM, where evaporation became anisotropic sooner and led to strong deformation (Fig. 2c). The resulting non-spherical shape of the supraparticles was always

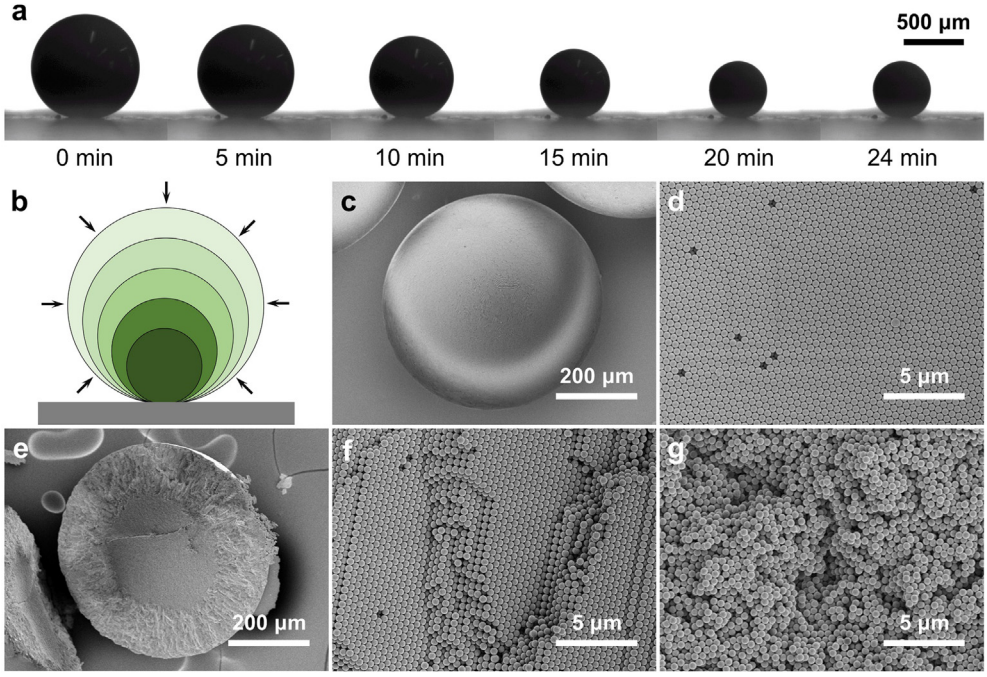

Fig. 1. PS supraparticles obtained after evaporation of PS colloid suspension droplets (22 °C at 32% relative humidity, the initial colloid volume fraction was 8% vol) on a superamphiphobic substrate. (a) Time evolution of particle shape. (b) Schematic illustration of the isotropic evaporation of droplets on a superamphiphobic surface. SEM top view of the spherical supraparticle (c) and the PS colloid ordering at the surface (d). (e-g) Cross-sectional SEM image (e), with crystalline shell (f) and random core (g) phases.

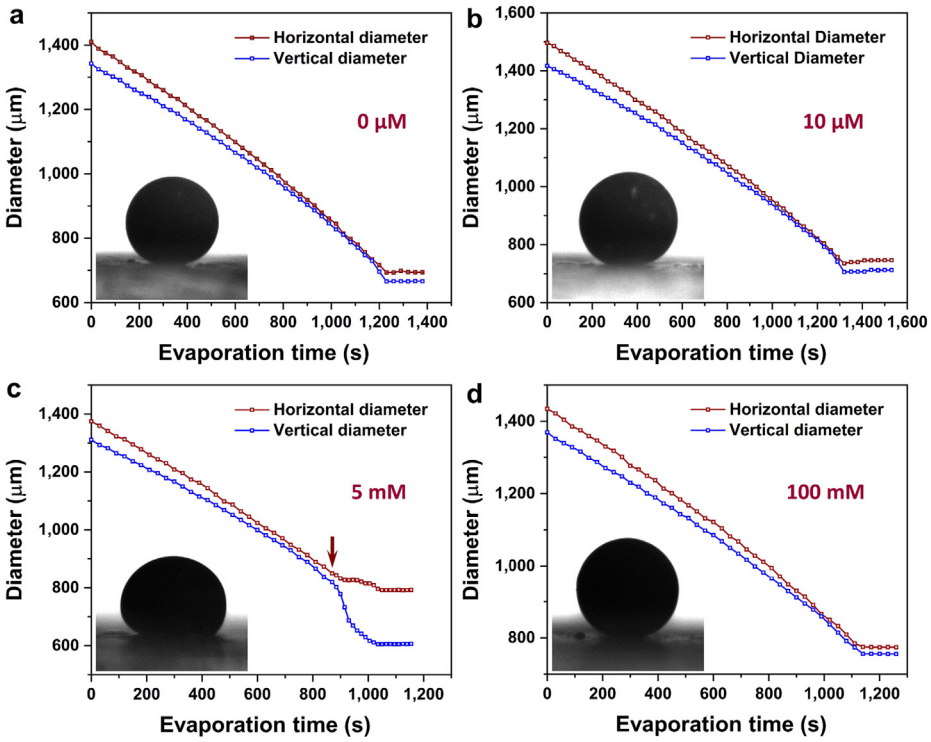

Fig. 2. Horizontal and vertical droplet diameter versus evaporation time for PS suspensions with different NaCl concentrations ("fast" evaporation at 22 ℃ and relative humidity RH = 32%). The concentrations of NaCl were 0 μM (a), 10 μM (b), 5 mM (c), and 100 mM (d). Insets are photographs of dried supraparticles. The arrow in (c) shows the onset of buckling.

due to deformation at the bottom facing the superamphiphobic surface. For a NaCl concentration of 500 μM, we observed just flattening of the bottom, while for concentrations of 1 mM to 10 mM, the supraparticles bulged inwards from the bottom side (Fig. S2i-k). However, at even higher salt concentrations of 50 mM and 100 mM, the evaporation changed back to an isotropic process, resulting in spherical supraparticles (Fig. 2d, Fig. S5l).

SEM characterization confirmed the structural changes with salt concentration (Fig. 3, S4 and S5). For concentrations below 500 μM, the crystallinity at the surface is maintained (Fig. 3b and S4d). However, the thickness of the crystalline shell decreases to 36–38% of the radius. When increasing the salt concentration further to 1–10 mM, the crystalline order at the surface decreases, and the thickness of the crystalline shell decreases further to 24% (1 mM), 21% (5 mM), and 1.2% (10 mM) of the supraparticle radius (compared to the largest radius of the supraparticles for the buckling cases), respectively (Fig. 3c-e). When increasing the salt concentration to 50 and 100 mM, the supraparticles recover their spherical shape. However, in these two cases, both the surface and interior of the supraparticles show a random distribution of the PS colloids without crystalline order (Fig. 3f and S4e), and no iridescence is observed (Fig. S3).

When we used $CaCl_2$ as the salt instead of NaCl, the shape and degree of crystallinity of the obtained supraparticles showed the same trends as those for NaCl. However, the onset of buckling and the transition from crystalline to amorphous structures occur at much lower concentrations (1 mM) of $CaCl_2$ compared to NaCl (Fig. S6).

To investigate the influence of evaporation speed on structure formation, we increased the relative humidity (RH ≈ 96%), which resulted in slower evaporation at a rate of 41 ± 0.6 $\mu m^2/s$ (T = 2 2 °C). The evaporation time increased from 24 min to 5 h. Again we observed a high degree of crystallinity at low salt concentrations and completely amorphous structures at high salt concentrations (Fig. S7, S8). However, there were also differences. First, for salt concentrations up to 100 μM, we observe crystalline order within the full supraparticle without any amorphous core. However, within this range, an increase in salt concentration induced an increase in the inner crystalline core with more short-range crystalline order (Fig. S7, c3-f3). Only at 500 μM NaCl can we clearly distinguish an outer crystalline shell and an inner amorphous core. Second, for salt concentrations of 5 mM and higher, the supraparticle exhibits a fully amorphous structure. Third, buckling is only observed for the 10 mM NaCl concentration, and the deviation from the spherical shape is much less pronounced than for the fast evaporation case; for 1 mM and 5 mM NaCl, only a slight flattening of the bottom was detected from the evaporation curves (Fig. S9).

3.2. Influence of salt on colloid interaction

To understand the influence of added salt on the final supraparticles, we must recall that the PS colloids in a suspension are stabilized due to their negative surface charge, which leads to electrostatic repulsion between them. The total interaction between the PS colloids is a combination of this electrostatic repulsion and attractive van der Waals forces.

The first positive term in Equation (1) describes the electrostatic repulsion, whereas the second negative term describes the van der Waals attraction between spherical colloids. The electrostatic repulsion decays exponentially with separation with a decay length given by the Debye length. The Debye length strongly depends on the salt concentration, as more ions in the electrolyte lead to a more effective screening of the surface charges. For the lowest salt concentrations of 1–10 μM NaCl, the true ionic strength of the solutions will most likely have been higher than that from

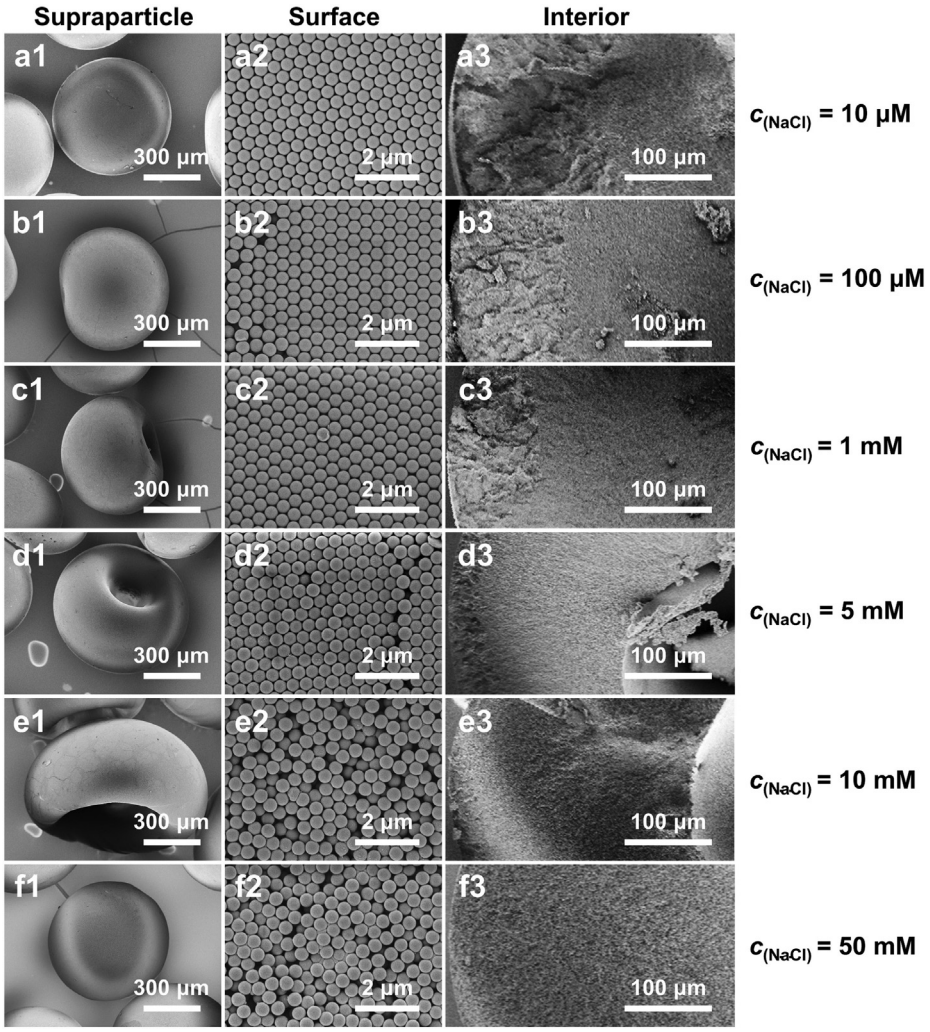

Fig. 3. Shape (1), surface structure (2), and cross-section (3) of supraparticles obtained by evaporating suspension droplets with different NaCl concentrations. The concentrations of NaCl were 10 µM (a), 100 µM (b), 1 mM (c), 5 mM (d), 10 mM (e), and 50 mM (f).

the added NaCl salt because trace amounts of ions, autodissociation of the water and dissolved CO_2 contribute as well. Therefore, the Debye length is expected to be on the order of approximately 100 nm for the lowest salt concentrations, approximately 10 nm for 1 mM NaCl, 3 nm for 10 mM NaCl, and approximately 1 nm for 100 mM NaCl.

To quantify the interaction between PS colloids, we directly measured the interaction between individual 4 µm PS particles using colloidal probe atomic force microscopy, where one colloid was attached to the AFM (atomic force microscopy) cantilever and one was immobilized on the surface. When the particles were brought closer together, there was a positive, repulsive force that was due to the electrostatic repulsion of the electrostatic double layer. Upon further approach, the repulsion dropped as the attractive van der Waals force to become dominant. Once the two particles were in hard contact, a strong repulsion was observed. By using fits of the experimental data with Equation (1), we extracted the Debye length and surface potential values. As the NaCl concentration increased, the Debye length decreased from approximately 14 nm (100 µM NaCl) to less than 2 nm (100 mM NaCl), whereas the surface potential decreased from more than −50 mV down to −20 mV. These two trends led to a strong reduction in the potential barrier with increasing salt concentration (Fig. 4 and S10).

With increasing salt concentration, the height of the potential barrier diminishes, and its position moves closer to zero. At some point, the repulsive barrier is no longer high enough, and the colloids come in contact, leading to irreversible adhesion due to the van der Waals interactions. Although forces were repulsive as colloids approached and came into contact, there was strong adhesion due to van der Waals attraction during retraction (Fig. S11). Therefore, colloids start to form agglomerates when the salt concentration exceeds a critical value. This can occur if the added salt concentration is high enough from the very beginning, as it was the case for the 100 mM NaCl salt concentration. But is will of course also happen when the salt concentration exceeds this critical value during evaporation as salt concentration increases with decreasing liquid volume, as it is ecpected for the intermediate salt concentrations.

3.3. Internal structures of supraparticles

During the evaporation of the colloidal suspension, several parallel processes contribute to the outcome: in the interior of the droplet, the colloids diffuse due to Brownian motion and are in random order. Close to the air–water interface, we have advection due to the shrinking interface, which pushes the colloids inwards. The relative ratio of diffusive motion and advection can be character-

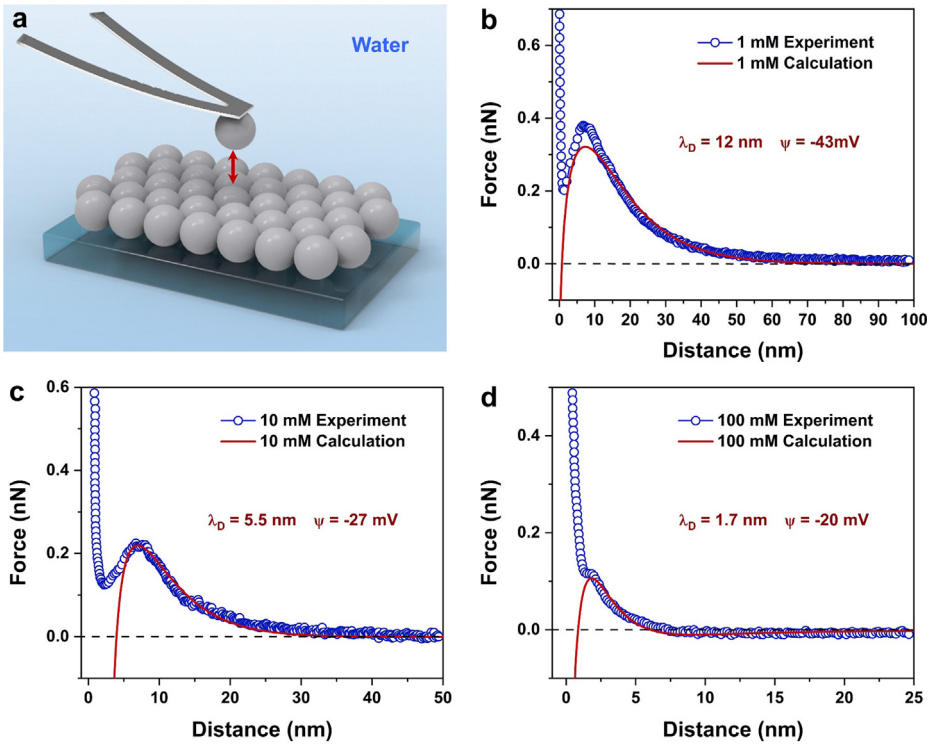

Fig. 4. Single colloid interaction forces. (a) Schematic of the colloidal probe AFM; (b-c) Single colloid interaction forces at different NaCl concentrations (1 mM, 10 mM, and 100 mM). Blue circles represent the experimental forces measured using colloid probe atomic force microscopy; Red lines represent the forces calculated according to the DLVO equation for the forces between two spheres. (For interpretation of the references to color in this figure legend, the reader is referred to the web version of this article.)

ized by the Peclet number (Pe), which is the ratio of diffusion and evaporation time constants for our system.

$$Pe = \tau_d/\tau_{ev} = \frac{1}{2}\left(\frac{3}{4\pi}\right)^{2/3}\frac{\alpha}{D_p} \quad (5)$$

Here, τ_d is the characteristic time that a dispersed particle needed to diffuse the distance of one initial droplet radius, τ_{ev} is the characteristic time of evaporation of a droplet, α is the evaporation speed and D_p is the diffusion coefficient of the colloids. For the case of fast (slow) evaporation at RH = 32% (RH = 96%), we obtain a Peclet number of Pe = 192 (Pe = 9.9). This means that diffusion is approximately 200 (10) times slower than the shrinking movement of the interface. Close to the interface, the colloids will therefore be enriched. The resulting high density of colloids causes the formation of a colloidal crystal in the outer layer during the early stage of evaporation. In these colloidal crystals, the colloids are not yet in contact due to strong electrostatic repulsion. This is in line with our observation that structural colors occur early in the drying process for low initial salt concentrations. As the drop is still evaporating isotropically during this phase, the mobility of colloids within the colloidal crystal must be high enough to allow this shell to reduce its surface area at the speed of the shrinking interface. In the late stage of the drying process, there will be a transition, where this outer layer of colloidal crystal (with the average surface-to-surface distance of the order of the Debye length) transitions into a solid crystal, where the colloids get into direct contact (Fig. 5a).

In the presence of salt, the average distance between the colloids in the colloidal crystal forming in the shell is smaller due to screening by the electric double layer. Therefore, the transition from a colloidal crystal to a solid shell occurs earlier, resulting in a reduction in the thickness of the crystalline shell with increasing salt concentration. When the shell solidifies, a significant volume in the center remains in the dispersed state and water continues to evaporate. This leads to capillary pressure caused by the liquid menisci formed between the colloids at the surface of the evaporating drop. This pressure difference inside can induce buckling of the outer shell (Fig. 5b), as observed for intermediate salt concentrations (red arrow in Fig. 2c). This phenomenon is similar to the drying of polymer solution when the outer shell formed by the polymer leads to buckling [54–56]. At this stage, part of the inner core has not yet formed a colloidal crystal. As the outer solidified shell suppresses advective motion, this driving force for densification and subsequent crystal formation is lacking. Therefore, the inner core will remain amorphous. In all cases where buckling or flattening of the supraparticles was observed, it occurred on the underneath. This indicates that even the slightly higher evaporation rate at the top side shifts the moment of crust formation in the shell for intermediate salt concentrations. For very high salt concentrations of 50 mM and 100 mM, the electrostatic repulsion is no longer strong enough to stabilize the colloidal dispersion. The colloids, therefore, start to form agglomerates in solution before the drying process (Fig. 5c). This process is enhanced as soon as the colloid density starts to increase. The formation of aggregates was confirmed in light scattering experiments, where we observed an increase in the hydrodynamic radius for salt concentrations of 50 mM and 100 mM (Fig. S12). Therefore, the formation of a colloidal crystal at the interface is no longer possible. It should be noted, that in our system, salt concentrations are too low to reach saturation conditions before the supraparticles have solidified: the interstitial volume between the PS colloids in the supraparticles is large enough to retain enough water to stay below saturation. Therefore, buckling of supraparticles is not related to salt crystallization as it was observed for the case of liquid marbles at order of magnitudes higher salt concentrations by Bormashenko et al. [57]. At such high salt concentrations, interfacial crystallization of NaCl may also play a role [53]. However, we can rule out the contribution of interfacial crystallization to buckling in our case:

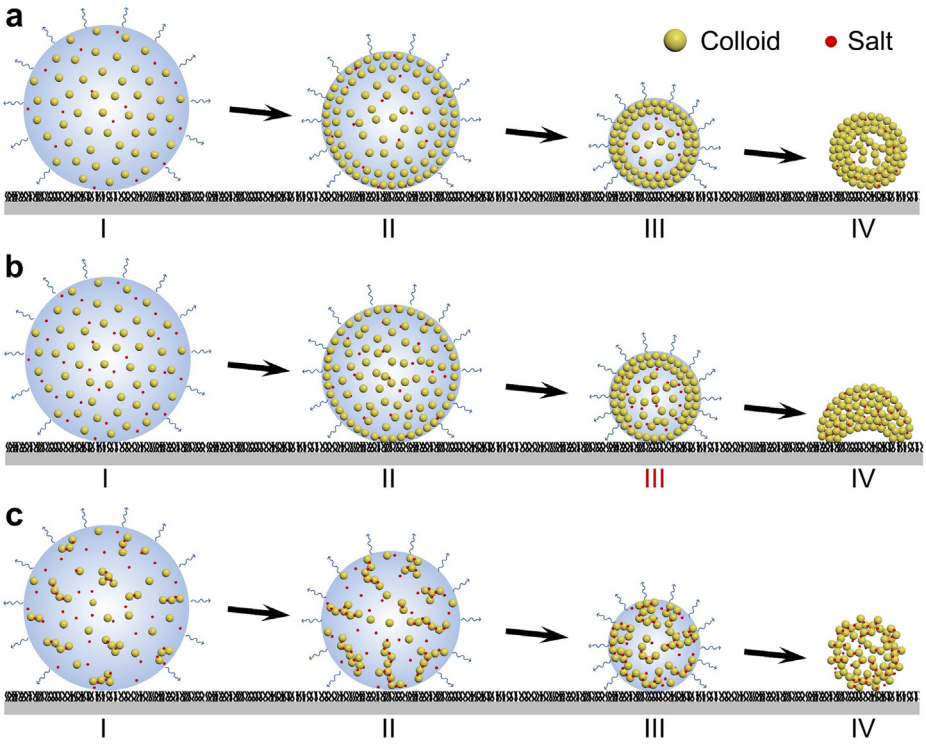

Fig. 5. Schematic of the colloids assembly behavior under low (a), medium (b) and high (c) salt concentrations.

first, buckling for our supraparticles only occurs at low salt concentrations but not at high ones, second, buckling occurs for $CaCl_2$ at much lower concentrations than for NaCl and third, SEM images do not show formation of any salt crystals in the buckled supraparticles–neither at the interface nor in the inside.

In addition to the dominant effect of salt concentration on supraparticle formation, the kinetics of the process is important. For the lower evaporation speed, we observed the formation of fully crystalline supraparticles at low salt concentrations without amorphous cores. Again, iridescence is seen in the early stage of evaporation. This indicates that advection is still strong enough to induce densification at the interface with the formation of a colloidal crystal. However, the slower shrinking of the interface leaves the system more time to equilibrate and reduces the likelihood of the transition from the colloidal crystal (with colloids still dispersed) to a solid crystal with direct contact that leads to the formation of an outer shell. Therefore, we observe neither an amorphous core nor buckling under slow evaporation. However, at higher salt concentrations, the final supraparticles show a lower degree of crystallinity. We attribute this reduced order to the fact that the system has more time for the formation of aggregates that hinder crystallization. Therefore, the formation of fully amorphous supraparticles was observed at salt concentrations of 5 mM, whereas for fast evaporation, fully amorphous supraparticles were observed at a 50 mM salt concentration.

3.4. Density and fracture strength of supraparticles

The degree of crystallinity within the supraparticles is important for their density and mechanical stability. Both parameters are essential for practical applications. Therefore, we estimated the density of the supraparticles from their final volume and the solid content of the original dispersion (Fig. S13). In addition, we tested the mechanical fracture strength of supraparticles (Fig. S15). We found solid fractions on the order of 60–65% even for fully crystalline supraparticles, indicating that highly dense hexagonal packing did not occur, even though the SEM images suggest long-range crystalline order on the outside. It appears that the density of the short-range crystalline cores of the supraparticles obtained by slow evaporation at low salt concentration was similar to that of the fully amorphous core for fast evaporation, while the density of the amorphous phase for slow evaporation was the lowest due to the longer agglomeration time. The fracture strength of the supraparticles was highest for the fully amorphous particles obtained at high salt concentrations. This is counterintuitive, as one might have expected that the particles with thick crystalline shells should be more stable. However, the highly crystalline supraparticles exhibited brittle fracture at lower forces, most likely due to fast crack propagation through the highly crystalline layer, once a crack is initiated at one of the defects (see supporting information).

4. Conclusions

On the basis of the previously reported evaporation approaches for supraparticle fabrication [2,29,39,40], this work demonstrated that the final morphology and interior structure of supraparticles could be controlled by regulating the colloidal interactions in suspension droplets with the addition of salt. The change of salt concentration could modulate the contribution of electrostatic repulsion and van der Waals attraction in colloid interaction, resulting in the variation of the supraparticles' morphology and interior structure. For NaCl concentrations below 100 μM, the final structure of the supraparticles was spherical and highly crystalline. With salt concentrations increasing up to 10 mM, the supraparticles were increasingly aspherical and less crystalline, similar to the morphology changes observed from evaporating silica droplets on superhydrophobic surface [42] and the aggregating behavior of charged colloids in suspension [58]. For NaCl concentrations of 50 mM and 100 mM, the supraparticles were spherical, which was not observed in previous work [42], but their inner structure was fully amorphous. Reducing the evaporation speed by increas-

ing the humidity favored crystallization at low salt concentrations, leading to fully crystalline supraparticles. However, for slow evaporation and 5 mM salt or more, the supraparticles were fully amorphous, while for fast evaporation, this fully amorphous state was found only for 50 mM and above.

By tuning the electrostatic interaction between primary colloids during evaporation on superamphiphobic surfaces, the external shape and the internal structure of the resulting supraparticles were controlled. The dependence on salt concentration and salt valency was correlated with the expected screening of the electrostatic repulsion between colloids. Increasing the salt concentration accelerated the aggregation of colloids, leading to a reduction in crystallization at low (micromoles) salt concentrations. At intermediate (millimoles) concentrations, an outer crystalline shell formed during evaporation led to buckling and non-spherical shapes in the final stage of evaporation. For high salt concentrations (tens of millimoles), the colloids aggregated at the initial evaporation stage, leading to spherical amorphous supraparticles. Therefore, the structure and physical properties of supraparticles can be modulated by the right combination of evaporation rate and salt concentration. This approach of tuning intercolloid forces to form supraparticles with different shapes and structures will allow us to fabricate supraparticles with specific structures (i.e., Janus, core–shell, disk, or doughnut-like), adjust their performance, and expand the application of supraparticle materials. Meanwhile, such an evaporation approach for supraparticle fabrication will open a new direction for interface science and broaden the applications of colloids.

Author Statement

W.L., M.K., and H.-J.B. conceived and designed the experiments. W.L. performed the experiments and characterizations. M.K. carried out the single colloid interaction forces measurement and result evaluation. W.S. conducted the PCS measurement and data analysis. W.L., M.K., W.S., and H.-J.B. co-wrote the paper. All authors discussed the results and commented on the manuscript.

Declaration of Competing Interest

The authors declare that they have no known competing financial interests or personal relationships that could have appeared to influence the work reported in this paper.

Acknowledgement

This work was supported by the Max Planck Center for Complex Fluid Dynamics, and the Fundamental Research Funds for the Central Universities (DUT21RC(3)078). W.L. thanks Dr. Arash Nikoubashman for helpful discussions. We also gratefully acknowledge Gabriele Schäfer for synthesizing the polystyrene colloids and Elke Muth for carrying out the Zeta-potential measurement.

Appendix A. Supplementary data

Supplementary data to this article can be found online at https://doi.org/10.1016/j.jcis.2021.09.035.

References

[1] S. Wintzheimer, T. Granath, M. Oppmann, T. Kister, T. Thai, T. Kraus, N. Vogel, K. Mandel, Supraparticles: Functionality from Uniform Structural Motifs, ACS Nano 12 (6) (2018) 5093–5120.
[2] W. Liu, M. Kappl, H.-J. Butt, Tuning the Porosity of Supraparticles, ACS Nano 13 (12) (2019) 13949–13956.
[3] B.D. Mattos, L.G. Greca, B.L. Tardy, W.L.E. Magalhães, O.J. Rojas, Green Formation of Robust Supraparticles for Cargo Protection and Hazards Control in Natural Environments, Small 14 (29) (2018) 1801256.
[4] F. Haque Khan, Chemical Hazards of Nanoparticles to Human and Environment (A Review), Orient. J. Chem. 29 (4) (2013) 1399–1408.
[5] H. Jafarizadeh-Malmiri, Z. Sayyar, N. Anarjan, A. Berenjian, Potential Hazards of Nanoparticles, in: H. Jafarizadeh-Malmiri, Z. Sayyar, N. Anarjan, A. Berenjian (Eds.), Nanobiotechnology in Food: Concepts, Applications and Perspectives, Springer, Cham, 2019, pp. 115–135.
[6] D. Luo, C. Yan, T. Wang, Interparticle Forces Underlying Nanoparticle Self-Assemblies, Small 11 (45) (2015) 5984–6008.
[7] R. Zhang, A.A. Elzatahry, S.S. Al-Deyab, D. Zhao, Mesoporous Titania: From Synthesis to Application, Nano Today 7 (4) (2012) 344–366.
[8] S. Li, J. Liu, N.S. Ramesar, H. Heinz, L. Xu, C. Xu, N.A. Kotov, Single- and Multi-Component Chiral Supraparticles as Modular Enantioselective Catalysts, Nat. Commun. 10 (1) (2019) 4826.
[9] K. Hou, J. Han, Z. Tang, Formation of Supraparticles and Their Application in Catalysis, ACS Materials Lett. 2 (1) (2020) 95–106.
[10] J. Liu, M. Xiao, C. Li, H. Li, Z. Wu, Q. Zhu, R. Tang, A.B. Xu, L. He, Rugby-Ball-Like Photonic Crystal Supraparticles with Non-Close-Packed Structures and Multiple Magneto-Optical Responses, J. Mater. Chem. C 7 (47) (2019) 15042–15048.
[11] D.-P. Song, T.H. Zhao, G. Guidetti, S. Vignolini, R.M. Parker, Hierarchical Photonic Pigments via the Confined Self-Assembly of Bottlebrush Block Copolymers, ACS Nano 13 (2) (2019) 1764–1771.
[12] M.B. Bigdeli, P.A. Tsai, Making Photonic Crystals *via* Evaporation of Nanoparticle-Laden Droplets on Superhydrophobic Microstructures, Langmuir 36 (17) (2020) 4835–4841.
[13] W. Wang, C. Hao, M. Sun, L. Xu, C. Xu, H. Kuang, Spiky Fe_3O_4@Au Supraparticles for Multimodal *in vivo* Imaging, Adv. Funct. Mater. 28 (22) (2018) 1800310.
[14] J. Yeom, P.P.G. Guimaraes, H.M. Ahn, B.-K. Jung, Q. Hu, K. McHugh, M.J. Mitchell, C.-O. Yun, R. Langer, A. Jaklenec, Chiral Supraparticles for Controllable Nanomedicine, Adv. Mater. 32 (1) (2020) 1903878.
[15] Y. Ma, C. Cortez-Jugo, J. Li, Z. Lin, R.T. Richardson, Y. Han, J. Zhou, M. Björnmalm, O.M. Feeney, Q.-Z. Zhong, C.J.H. Porter, A.K. Wise, F. Caruso, Engineering Biocoatings to Prolong Drug Release from Supraparticles, Biomacromolecules 20 (9) (2019) 3425–3434.
[16] F. Montanarella, T. Altantzis, D. Zanaga, F.T. Rabouw, S. Bals, P. Baesjou, D. Vanmaekelbergh, A. van Blaaderen, Composite Supraparticles with Tunable Light Emission, ACS Nano 11 (9) (2017) 9136–9142.
[17] H.J. Koo, Y.J. Kim, Y.H. Lee, W.I. Lee, K. Kim, N.G. Park, Nano-Embossed Hollow Spherical TiO_2 as Bifunctional Material for High-Efficiency Dye-Sensitized Solar Cells, Adv. Mater. 20 (1) (2008) 195–199.
[18] J.W. Yoo, K. Zhang, V. Patil, J.T. Lee, D.-W. Jung, L.S. Pu, W. Oh, W.-S. Yoon, J.H. Park, G.-R. Yi, Porous Supraparticles of $LiFePO_4$ Nanorods with Carbon for High Rate Li-Ion Batteries, Mater. Express 8 (4) (2018) 316–324.
[19] X. Zhou, Z. Li, X. Deng, B. Yan, Z. Wang, X. Chen, S. Huang, High Performance Perovskite Solar Cells Using Cu_9S_5 Supraparticles Incorporated Hole Transport Layers, Nanotechnology 30 (44) (2019) 445401.
[20] T. Wang, D. LaMontagne, J. Lynch, J. Zhuang, Y.C. Cao, Colloidal Superparticles from Nanoparticle Assembly, Chem. Soc. Rev. 42 (7) (2013) 2804–2823.
[21] F. Montanarella, D. Urbonas, L. Chadwick, P.G. Moerman, P.J. Baesjou, R.F. Mahrt, A. van Blaaderen, T. Stöferle, D. Vanmaekelbergh, Lasing Supraparticles Self-Assembled from Nanocrystals, ACS Nano 12 (12) (2018) 12788–12794.
[22] S. Mi, Y. Xie, Y. Li, R. Liu, X. Liu, I.I. Smalyukh, Z. Chen, The Effect of Thickness-Tunable ZrO_2 Shell on Enhancing the Tunneling Magnetoresistance of Fe_3O_4 Supraparticles, Adv. Mater. Interfaces 5 (12) (2018) 1800236.
[23] D. Maiolo, C. Pigliacelli, P. Sánchez Moreno, M.B. Violatto, L. Talamini, I. Tirotta, R. Piccirillo, M. Zucchetti, L. Morosi, R. Frapolli, G. Candiani, P. Bigini, P. Metrangolo, F. Baldelli Bombelli, Bioreducible Hydrophobin-Stabilized Supraparticles for Selective Intracellular Release, ACS Nano 11 (9) (2017) 9413–9423.
[24] T. Bollhorst, S. Jakob, J. Köser, M. Maas, K. Rezwan, Chitosan Supraparticles with Fluorescent Silica Nanoparticle Shells and Nanodiamond-Loaded Cores, J. Mater. Chem. B 5 (8) (2017) 1664–1672.
[25] D. Wang, T. Xie, Q. Peng, Y. Li, Ag, Ag_2S, and Ag_2Se Nanocrystals: Synthesis, Assembly, and Construction of Mesoporous Structures, J. Am. Chem. Soc. 130 (12) (2008) 4016–4022.
[26] S.I. Lim, C.-J. Zhong, Molecularly Mediated Processing and Assembly of Nanoparticles: Exploring the Interparticle Interactions and Structures, Acc. Chem. Res. 42 (6) (2009) 798–808.
[27] S.A. Jenekhe, X.L. Chen, Self-Assembled Aggregates of Rod-Coil Block Copolymers and Their Solubilization and Encapsulation of Fullerenes, Science 279 (5358) (1998) 1903.
[28] F. Bai, D. Wang, Z. Huo, W. Chen, L. Liu, X. Liang, C. Chen, X. Wang, Q. Peng, Y. Li, A Versatile Bottom-up Assembly Approach to Colloidal Spheres from Nanocrystals, Angew. Chem. Int. Ed. 46 (35) (2007) 6650–6653.
[29] V. Rastogi, S. Melle, O.G. Calderón, A.A. García, M. Marquez, O.D. Velev, Synthesis of Light-Diffracting Assemblies from Microspheres and Nanoparticles in Droplets on a Superhydrophobic Surface, Adv. Mater. 20 (22) (2008) 4263–4268.
[30] M. Sperling, M. Gradzielski, Droplets, Evaporation and a Superhydrophobic Surface: Simple Tools for Guiding Colloidal Particles into Complex Materials, Gels 3 (2017) 15.
[31] J.M. Stauber, S.K. Wilson, B.R. Duffy, Evaporation of Droplets on Strongly Hydrophobic Substrates, Langmuir 31 (12) (2015) 3653–3660.
[32] Z. Pan, S. Dash, J.A. Weibel, S.V. Garimella, Assessment of Water Droplet Evaporation Mechanisms on Hydrophobic and Superhydrophobic Substrates, Langmuir 29 (51) (2013) 15831–15841.

[33] Z. Chu, S. Seeger, Superamphiphobic Surfaces, Chem. Soc. Rev. 43 (8) (2014) 2784–2798.
[34] K. Ellinas, A. Tserepi, E. Gogolides, Durable Superhydrophobic and Superamphiphobic Polymeric Surfaces and Their Applications: A Review, Adv. Colloid Interface Sci. 250 (2017) 132–157.
[35] H. Liu, Y. Wang, J. Huang, Z. Chen, G. Chen, Y. Lai, Bioinspired Surfaces with Superamphiphobic Properties: Concepts, Synthesis, and Applications, Adv. Funct. Mater. 28 (19) (2018) 1707415.
[36] J. Zhou, X. Man, Y. Jiang, M. Doi, Structure Formation in Soft-Matter Solutions Induced by Solvent Evaporation, Adv. Mater. 29 (45) (2017) 1703769.
[37] D. Mampallil, H.B. Eral, A Review on Suppression and Utilization of the Coffee-Ring Effect, Adv. Colloid Interface Sci. 252 (2018) 38–54.
[38] A.D. Nikolov, D.T. Wasan, P. Wu, Marangoni Flow Alters Wetting: Coffee Ring and Superspreading, Curr. Opin. Colloid Interface Sci. 51 (2021) 101387.
[39] W. Liu, J. Midya, M. Kappl, H.-J. Butt, A. Nikoubashman, Segregation in Drying Binary Colloidal Droplets, ACS Nano 13 (5) (2019) 4972–4979.
[40] S. Wooh, H. Huesmann, M.N. Tahir, M. Paven, K. Wichmann, D. Vollmer, W. Tremel, P. Papadopoulos, H.-J. Butt, Synthesis of Mesoporous Supraparticles on Superamphiphobic Surfaces, Adv. Mater. 27 (45) (2015) 7338–7343.
[41] H. Tan, S. Wooh, H.-J. Butt, X. Zhang, D. Lohse, Porous Supraparticle Assembly Through Self-Lubricating Evaporating Colloidal Ouzo Drops, Nat. Commun. 10 (1) (2019) 478.
[42] M. Sperling, O.D. Velev, M. Gradzielski, Controlling the Shape of Evaporating Droplets by Ionic Strength: Formation of Highly Anisometric Silica Supraparticles, Angew. Chem. Int. Ed. 53 (2) (2014) 586–590.
[43] G.T.D. Shouldice, G.A. Vandezande, A. Rudin, Practical Aspects of the Emulsifier-Free Emulsion Polymerization of Styrene, Eur. Polym. J. 30 (2) (1994) 179–183.
[44] J. Zhang, S. Seeger, Superoleophobic Coatings with Ultralow Sliding Angles Based on Silicone Nanofilaments, Angew. Chem. Int. Ed. 50 (29) (2011) 6652–6656.
[45] F. Geyer, C. Schönecker, H.-J. Butt, D. Vollmer, Enhancing CO_2 Capture using Robust Superomniphobic Membranes, Adv. Mater. 29 (5) (2017) 1603524.
[46] M. Kappl, H.-J. Butt, The Colloidal Probe Technique and Its Application to Adhesion Force Measurements, Part. Part. Syst. Charact. 19 (3) (2002) 129–143.
[47] J.L. Hutter, J. Bechhoefer, Calibration of Atomic-Force Microscope Tips, Rev. Sci. Instrum. 64 (7) (1993) 1868–1873.
[48] H. Ohshima, Electrostatic Interaction between Two Dissimilar Spheres: An Explicit Analytic Expression, J. Colloid Interface Sci. 162 (2) (1994) 487–495.
[49] Fernández-Barbero, A.; Martín-Rodríguez, A.; Callejas-Fernández, J.; Hidalgo-Alvarez, R., On the Calculation of Electrokinetic Potential and Hamaker Constant of Model Colloids. J. Colloid Interface Sci. 1994, 162 (1), 257-260.
[50] A.M. Smith, M. Borkovec, G. Trefalt, Forces between Solid Surfaces in Aqueous Electrolyte Solutions, Adv. Colloid Interface Sci. 275 (2020) 102078.
[51] A. Marin, S. Karpitschka, D. Noguera-Marín, M.A. Cabrerizo-Vílchez, M. Rossi, C.J. Kähler, M.A. Rodríguez Valverde, Solutal Marangoni Flow as the Cause of Ring Stains from Drying Salty Colloidal Drops, Phys. Rev. Fluid. 4 (4) (2019) 041604(R).
[52] Picknett, R. G.; R., B., The Evaporation of Sessile or Pendant Drops in Still Air. J. Colloid Interface Sci. 1977, 61, 336-350.
[53] P. Kumar Roy, I. Legchenkova, S. Shoval, E. Bormashenko, Interfacial Crystallization within Janus Saline Marbles, J. Phys. Chem. C. 125 (2) (2021) 1414–1420.
[54] T. Kajiya, E. Nishitani, T. Yamaue, M. Doi, Piling-to-Buckling Transition in the Drying Process of Polymer Solution Drop on Substrate Having a Large Contact Angle, Phys. Rev. E 73 (1) (2006) 011601.
[55] Y. Shimokawa, T. Kajiya, K. Sakai, M. Doi, Measurement of the Skin Layer in the Drying Process of a Polymer Solution, Phys. Rev. E 84 (5) (2011) 051803.
[56] Okuzono, T.; Ozawa, K. y.; Doi, M., Simple Model of Skin Formation Caused by Solvent Evaporation in Polymer Solutions. Phys. Rev. Lett. 2006, 97 (13), 136103.
[57] E. Bormashenko, P. Kumar Roy, S. Shoval, I. Legchenkova, Interfacial Crystallization within Liqiud Marbles, Condens. Matter 5 (4) (2020) 62.
[58] A. Murakado, A. Toyotama, M. Yamamoto, R. Nagano, T. Okuzono, J. Yamanaka, Thermoreversible Crystallization of Charged Colloids due to Adsorption/Desorption of Ionic Surfactants, J. Colloid Interface Sci. 465 (2016) 200.